

Effect of net direct current on the properties of radio frequency sheaths: simulation and cross-code comparison

J. R. Myra,¹ M.T. Elias,² D. Curreli,² and T. G. Jenkins³

¹*Lodestar Research Corporation, Boulder, Colorado 80301, USA*

²*University of Illinois at Urbana-Champaign, Urbana, Illinois, 61821 USA*

³*Tech-X Corporation, Boulder, Colorado, 80303 USA*

July 2020 revised October 2020

submitted to
Nuclear Fusion

DOE-ER/54392-97; ORNL/4000158507-6

LRC-20-186

LODESTAR RESEARCH CORPORATION

*2400 Central Avenue
Boulder, Colorado 80301*

Effect of net direct current on the properties of radio frequency sheaths: simulation and cross-code comparison

J. R. Myra,¹ M.T. Elias,² D. Curreli,² and T. G. Jenkins³

¹*Lodestar Research Corporation, 2400 Central Ave. Suite P-5, Boulder, Colorado, 80301 USA*

²*University of Illinois at Urbana-Champaign, 104 S. Wright St, Urbana, Illinois, 61821 USA*

³*Tech-X Corporation, 5621 Arapahoe Avenue Suite A, Boulder, Colorado, 80303 USA*

Abstract

In order to understand, predict and control ion cyclotron range of frequency (ICRF) interactions with tokamak scrape-off layer plasmas, computational tools which can model radio frequency (RF) sheaths are needed. In particular, models for the effective surface impedance and DC rectified sheath potentials may be coupled with full wave RF simulation codes to predict self-consistent wave fields near surfaces and the resulting power dissipation and plasma-material interactions from ion sputtering. In this study, previous work assuming zero net DC current flow through the sheath is generalized to allow the surface to collect net positive or negative current, as is often observed in experiments. The waveforms, DC potential and RF admittance are investigated by means of analytical theory, nonlinear fluid and particle-in-cell (PIC) codes. Cross-code comparisons provide detailed model verification and elucidate the roles of ion and electron kinetics. When the sheath draws negative (positive) DC current, the voltage rectification is reduced (increased) compared with the zero-current case, and the magnitude of both the real and imaginary parts of the admittance are increased (reduced). A previous four-input parametrization of the sheath rectification and admittance properties is generalized to include a fifth parameter describing the DC sheath current.

Keywords: radio-frequency, sheath, simulation, verification, impedance, rectification, ICRF, tokamak

1. Introduction

Radio frequency (RF) waves in the ion cyclotron range of frequencies (ICRF) are expected to play an increasingly important role as tokamak research progresses towards the reactor regime. Waves in this frequency regime can provide robust and cost-effective heating for present day and future devices. However, there are some regimes in which unwanted interactions of ICRF wave fields with the antenna and/or boundary plasma are observed. [1-11] It is commonly thought that RF sheaths are responsible for many of these unwanted interactions. A short review of RF sheath physics may be found in Refs. [12,13]. RF sheaths increase the plasma potential relative to the wall, enhancing the energy of ions impacting the surface, and therefore increase sputtering and erosion. [14]

Learning how to model, quantitatively predict and ultimately control the magnitude of RF sheath interactions for a given set of conditions is an important challenge facing the theory and numerical simulation communities, and one that has received considerable attention. [15-24] Sheaths exist on a short spatial scale, nominally the Debye scale, which is generally small in fusion-relevant devices compared with RF wavelengths and device-size scale lengths. This makes it possible to divide the RF sheath problem into a micro-scale problem on the Debye scale of the sheath itself, and a macro-scale problem on the global scale of the waves. The two scales may then be self-consistently patched together using appropriate boundary conditions (BCs). [24,25] The global RF problem requires electromagnetic BCs which may be given in the form of an effective surface impedance at the sheath entrance, replacing the more commonly used zero-impedance, perfectly conducting wall BC. On the other hand, the micro-scale RF sheath problem requires the amplitude of the RF waves which may be given as the RF potential difference between the plasma and the wall. From this information and the plasma and magnetic field parameters the micro-scale problem may be solved to obtain the RF currents flowing through the sheath, hence the RF sheath impedance. [25,26] Additionally, the micro-scale solution provides the DC “rectified” potential that is needed for sputtering calculations.

The present paper is focused on the micro-scale problem and generalizes some previous work on the sheath potential and impedance. In that previous work [25,26] it was assumed that there was no DC current flowing through the sheath. In fact, RF driven DC currents flowing between active and passive component were first (as far as we know) observed on the TEXTOR tokamak [27] and have since been observed in many other experiments including the AUG [28], NSTX [29] and EAST [30] tokamaks, as well as in the LAPD linear device [31]. This is not surprising since RF voltage rectification creates a large DC potential difference between the plasma and the wall. In the present paper, we allow the surface to collect net positive or negative DC current and study the effect of this current on the DC plasma potential and on the sheath impedance.

Ultimately, in experiments, the DC current circuit is completed in both the plasma and the vessel walls; from a modeling perspective the circuit should be made self-consistent with the plasma potential through a global transport code. This global DC or slow time-scale problem is separate from the global RF problem. Both global problems provide motivation for this paper but are beyond its scope. The interested reader is referred to some initial semi-qualitative models on RF-induced DC current flow such as used to explain mixed phasing experiments on JET [32], asymmetric heat loads on Tore Supra [4, 33] and the transverse and parallel structure of DC potentials in the presence of asymmetric sheaths. [34,35] In JET an asymmetric interaction was observed on differently phased antennas that depended on their relative powering. [32] This was interpreted in a heuristic model which invoked the generation of parallel currents by RF sheath voltage asymmetry and the radial flow of these current around limiters. In Tore Supra, when the power splitting between left and right antenna current straps was unbalanced, heat flux asymmetries between the two surface contact points of a field line were observed. [4] These asymmetries were modeled by considering RF sheath-driven DC currents flowing between the contact points, taking into account both parallel and transverse DC conductivity. However, much of the modeling work in Refs. [15-24] does not yet take DC currents into account.

Although an investigation of the effect of DC current on RF sheaths was the initial motivation for the work described in this paper, our paper also contains some important cross-code benchmarking work. In addition to the nonlinear fluid code NoFlu which was also used in previous micro-scale sheath studies, the present paper presents results from the particle in cell codes hPIC [36,37] and Vorpil [38]. Cross-code benchmarking of these codes is provided for verification purposes and also to elucidate to what extent kinetic physics of both ions and electrons impacts the results of the calculations. In particular hPIC is used to generalize NoFlu's cold ion fluid model while Vorpil generalizes the Maxwell-Boltzmann electron model that was used in this work by both NoFlu and hPIC.

Finally, for practical implementation of a sheath BC in global RF codes, a robust module must be able to return the sheath impedance and DC plasma potential quickly and accurately, for any set of validated input parameters. While in principle the impedance can be calculated using the codes just mentioned, in practice there may be convergence difficulties or the need to hand-tune numerical parameters such as system size, time and space resolution. For these reasons it is beneficial, if not necessary, to have tabulations or parametrized fits of pre-computed results for the sheath impedance and DC plasma potential. This was achieved previously [26] for the case of four dimensionless input parameters: the degree of sheath magnetization, the magnetic field angle with the surface, a normalized RF field strength and the degree of ion mobility set by the wave frequency. In the present paper we add a fifth dimensionless parameter for the DC current. Using

analytical arguments, the previous parametrized fits [26] are generalized and the results are compared with results from the NoFlu code.

The plan of our paper is as follows. In Sec. 2 the model geometry is presented, and the codes are described. A procedure is outlined for comparing the results of these codes that takes into account differences in how inputs are specified. Unless otherwise stated, results in this paper are given in terms of dimensionless parameters, which are also introduced in Sec. 2. Section 3 contains the numerical results that characterize the effect of the DC current on the RF sheath properties. In this section, cross-code benchmarking between NoFlu, hPIC and Vorpal is presented for a variety of cases both with and without DC current flow. Kinetic ion effects are discussed in Sec. 3.2 and kinetic electron effects in Sec. 3.3. In Sec. 4 analytical results and parametrization fits are given to encapsulate the effect of the DC sheath current. The quality of these fits is assessed. Some points of discussion are given in Sec. 5. Finally, in Sec. 6 a summary of key results and our conclusions are presented. This paper extends a much shorter and more focused conference paper on similar topics. [39]

2. Model

2.1. Model geometry and circuit

The geometry and circuit are illustrated in figure 1. We consider a double-plate model of the type employed in Refs. [25,26], namely, a plasma-filled “capacitor” immersed in an oblique angle magnetic field, driven by anti-symmetric RF voltages on each of the two plates. Particle and DC current sources are located at the midplane $x = L$ of the capacitor cell. The distance between the plates is large compared with both the Debye length and the ion Larmor radius, so that the sources exist in the upstream region outside the non-neutral sheath and magnetic presheath. The model is 1D with all quantities varying only in x , the direction normal to the plates. Similar double sheath models have been considered by many other authors. See for example Refs. [34, 40] and references therein.

The applied voltages on plates 1 and 2 are $V_1 = -V_{rf} \cos \omega t$ and $V_2 = V_{rf} \cos \omega t$ respectively. Thus, the plates are at a DC potential of zero. In the absence of a DC current source, RF sheath rectification causes the DC upstream plasma potential Φ_0 to rise to a value of order V_{rf} when $eV_{rf} \gg 3T_e$. The dependence of Φ_0 on the dimensionless parameters of the problem, including now, the DC current flowing through the sheath, is one of the desired outputs of the calculation. The other quantity of interest is the sheath admittance parameter z defined as a normalized ratio of the RF current density flowing through the sheath to the RF voltage across the sheath at frequency ω . Because the admittance parameter $y = 1/z$ is additive in the ion, electron and displacement currents for this voltage driven problem, it is more convenient to calculate it rather than the impedance.

The considered problem has definite symmetries about the midplane $x = L$. The mathematical form of these symmetries, involving both space and time transformations, is given in Ref. 25. The main point of interest here is that we may view the left sheath (at plate 1) as being driven by an applied RF and DC voltage difference between the upstream location ($x = L$) and the plate with a response in the form of RF and DC currents. In fact, it is more convenient to *specify* the DC current and *measure* the DC voltage from the simulation, and that is what is done here. Furthermore, because the micro-scale sheath problem is electrostatic, the RF voltage applied to the plates here is mathematically equivalent to having RF grounded plates and an upstream RF voltage source. This corresponds to a one-sided sheath model.

The rectification and admittance properties of the left sheath are therefore *almost* isolated from the right sheath and independent of how the system is driven – almost, because, as we will see, the presence of the right sheath in this model does influence the harmonics at 2ω , 4ω , ... of the electrostatic potential Φ_0 generated at the upstream (midplane) location. Communication of the electron current, and hence the potential, between the two plates is possible because Maxwell-Boltzmann electrons respond instantaneously. On the other hand, the displacement and ion currents in the two sheaths are essentially uncoupled. Information flow in the ion channel is always outgoing (i.e. towards the plates) because of the outgoing sonic flow, and there is negligible capacitive coupling between the sheaths at the left- and right-hand sides as long as the sheath widths are small compared with the domain size. Consequently, for present purposes, the symmetric double plate model is more generally useful than might otherwise appear.

It should again be emphasized that the point of this paper is the microscale sheath properties, i.e. sheath rectification and sheath impedance as a function of a presumed known DC current. Asymmetry plays an important role in the macroscale problem which *determines* the DC current. [32-34].

2.2. Numerical model: code descriptions

To study the properties of the sheath in this system we employ three numerical codes in this paper: a fluid code NoFlu, and the PIC codes hPIC and Vorpak. A brief description of each code follows.

NoFlu is a one-dimensional nonlinear fluid code that invokes the cold ion approximation and the isothermal Maxwell-Boltzmann electron model. The fundamental equations of the model are Poisson's equation for the electrostatic potential Φ , the Maxwell-Boltzmann relation for electron density n_e and the electron current density to the sheath J_e , the continuity equation for ion density n_i , and the three components of the ion momentum equation of motion under the Lorentz force. These equations are given explicitly in Sec. 2.4 where the dimensionless variables of the problem are also discussed. The code discretizes in space and time, but instead of marching forward in time, NoFlu solves for all time points within a single RF period simultaneously and

implicitly. Typical resolutions employed for the runs in this paper are 20 to 60 time points per RF period, and 50 spatial points across the half domain (symmetry is employed), approximately two per Debye length. The actual time and space points are illustrated by the small dots visible for the NoFlu curves in figures 2 and 4-7. The NoFlu model employed here is identical to the version described in Ref. 25 except for the addition of an upstream DC current source at the midplane. The code is implemented in *Mathematica* where a typical run completes in 1 to 5 min (serial CPU) and requires 70 MB of RAM.

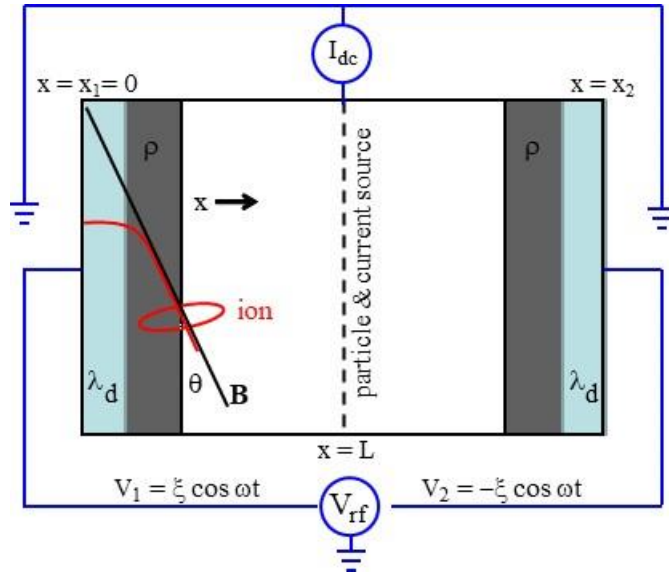


Figure 1. Symmetric dual plate RF sheath model. Plasma fills the interior region. The plates are DC grounded and RF driven π out of phase with amplitude ξ . In the illustrated case applicable to the NoFlu model (see Sec. 2.2), particle and current sources are located at the midplane $x = L$ where the imposed ion parallel flow velocity towards the plates is taken to be slightly greater the sound speed. The hPIC and Vorpal models use distributed particle and current sources described in the main text.

The hPIC code [36,37] is an electrostatic Particle-in-Cell application targeted at large-scale simulations of plasma–material interactions. The code can simulate multi-component strongly-magnetized plasmas in a region close to the wall, including the magnetic sheath and presheath. The code has been adapted to include oscillating boundary conditions to analyze RF sheath problems. For the conditions relevant to this work, hPIC operates with fully-kinetic ions and nonlinear Boltzmann electrons in the Poisson problem. The hPIC code implements the charge conservation algorithm recently developed and detailed in Ref. [41]. The DC current is added to the charge conservation algorithm. A volumetric ionization source is used to replenish the particles lost to the walls. The ionization rate is tuned to maintain charge conservation in the plasma domain

and thus maintain a constant average particle density in the plasma domain. hPIC provides the energy-angle distributions of the ions leaving the domain and impacting the walls, offering the opportunity to couple the code to plasma-material interaction codes [42,43]. Here we consider a 1D3V symmetric plate-to-plate collisionless hydrogen plasma configuration in a finite-size domain of length 3 cm with magnetic field $B = 1\text{T}$ parallel to the surface normal and volume averaged plasma density of $5 \times 10^{16} \text{ m}^{-3}$. The numerical discretization was set at 2 nodes per Debye length and 20 timesteps per ion gyroperiod (determined from previous work to be a suitable simulation parameter regime). A domain size of at least 50 Debye lengths is required to capture the RF sheath formation for these parameters; a larger domain does not affect the results. The plates oscillate at $V = \pm (V_{\text{pp}}/2) \cos \omega t$ volts where V_{pp} is the peak-to-peak RF voltage. The RF frequency of our low frequency case is $\omega = 1.47 \times 10^8 \text{ s}^{-1}$ yielding a volume averaged $\omega/\omega_{\text{pi}} = 0.5$. For the hPIC cases in this paper, a typical run time is 2 to 7 min (serial CPU) and the code requires about 50 MB RAM for a simulation with 10^6 particles.

Vorpal [38] is a massively parallel kinetic electromagnetics code based on finite-difference (FDTD) and particle-in-cell (PIC) methods. The Vorpal simulations performed for this paper used a PIC representation for both ions and electrons in the electrostatic approximation, contained between two infinite plates separated by 200 Debye lengths. Other parameters are the same as above and the case $V_{\text{pp}} = 200 \text{ V}$ is simulated. Numerically, the simulation grid resolves the Debye length (six grid cells per Debye length) and electron gyromotion (20 timesteps per gyro-orbit); with 10-500 particles per grid cell. For the Vorpal simulations, higher spatial resolution than hPIC was required due to the density and temperature variation introduced by kinetic electrons; the use of six grid cells per Debye length (defined relative to the initial electron load density and temperature) was shown to demonstrate suitable numerical convergence. In initial simulation efforts, particles lost to the wall were re-loaded into the domain on the following timestep to maintain the average species densities. However, this method exhibited considerable numerical noise and/or instability. To circumvent these issues, we instead added particles of both species into the domain at a fixed rate. The simulations were run until steady-state was achieved; the desired average steady-state density of $5 \times 10^{16} \text{ m}^{-3}$ can be obtained by adjustment of the loading rate. DC current injection can be achieved by altering the loading rate of one species relative to the other (though this approach was not used in the work presented here). Because the Vorpal simulations represent the electron distribution function kinetically, they are constrained to small time-steps so that the electron motion can be resolved. Realistic electron mass is employed. Computational requirements for these runs are thus greater than for the corresponding hPIC runs: the Vorpal runs presented here use 1.9×10^5 particles, take 7.2 million timesteps and run for 96 hours (serial) of wall-clock time despite only modest RAM requirements ($< 20 \text{ MB}$).

2.3. Procedure for cross code comparison

Cross-code comparisons are complicated by the different ways that particles are sourced in the codes. NoFlu has a local upstream particle source with an imposed sonic ion parallel flow velocity. As a result, there is no source presheath in the NoFlu simulations and the specified upstream ion (and electron) density is also the density at the entrance to the sheath region. This is the density parameter that is ultimately required when the sheath BC is applied in global RF codes.

In contrast hPIC and Vorpal impose distributed particle sources. Although the particle source rate controls the density, neither the density at the entrance to the sheath, nor the DC current flowing through the sheath are known a priori. Therefore, a procedure has been established for cross-code comparison between hPIC or Vorpal and NoFlu. (A similar procedure is used for the both codes, but described in the following for hPIC.) First, hPIC is run for parameters that approximate the desired density and DC current. The hPIC results are then post-processed to obtain the actual DC *ion* current flowing to one of the plates, $J_{i0,hPIC}$. In NoFlu at the sheath entrance the DC *ion* current flowing to the plate is $J_{i0} = n_{i0} e u_{||0}$ where $u_{||0}$ is the upstream source velocity of the ions. (Here $|u_{||0}| = 1.1 c_s$ comfortably above the cold ion Bohm velocity where $c_s = (T_e/m_i)^{1/2}$ is the cold ion sound speed.) The effective density at the sheath entrance is then given by $n_{i0} = J_{i0,hPIC}/(e u_{||0})$. This value of density is used to set the dimensionless input parameters for the NoFlu comparison run. The net DC (total) current collected at the plate is also post-processed from hPIC and normalized for input into NoFlu using the same density.

As we will see, the procedure just outlined allows for excellent comparative agreement between the results of the different codes. This is in spite of the facts that: (i) finite T_i changes the sound speed and the Bohm velocity, and the PIC codes employed $T_i \geq T_e$, and (ii) the upstream locations of the source, the source models and the presheaths are different for the different codes.

2.4. Nonlinear fluid equations and dimensionless variables

In this paper, unless otherwise explicitly indicated, results will be presented in the dimensionless variables of the NoFlu model, where time is normalized to the reference upstream inverse ion plasma frequency $1/\omega_{pi0}$ and spatial dimensions are normalized to the reference electron Debye length λ_{de0} . The density is normalized to the upstream quasi-neutral density n_{i0} at the sheath entrance and RF voltages are normalized to T_e/e where T_e is the electron temperature, assumed to be constant. These units are natural ones for sheath dynamics, and result in velocities normalized to the ion sound speed $c_s = \lambda_{de0}\omega_{pi0}$. The corresponding dimensional equations and sheath impedance are given in Ref. 25. In particular, the admittance per unit area of a surface in SI units is given by $y_{SI} = y (\epsilon_0 \omega_{pi}/\lambda_d)$ where y is the dimensionless admittance parameter discussed in this paper and defined in Eq. (7).

The fundamental equations of the NoFlu model in dimensionless variables are:

$$\frac{\partial^2 \Phi}{\partial x^2} = -(n_i - n_e) \quad (1)$$

$$n_e = \exp(\Phi - \Phi_0) \quad (2)$$

$$\frac{\partial n_i}{\partial t} + \frac{\partial}{\partial x}(n_i u_x) = 0 \quad (3)$$

$$\left(\frac{\partial}{\partial t} + u_x \frac{\partial}{\partial x} \right) \mathbf{u} = -\nabla \Phi + \Omega \mathbf{u} \times \mathbf{b} \quad (4)$$

Here x is the spatial variable normal to the plate with $x = 0$ at the metal surface, \mathbf{b} is the unit vector in the direction of the magnetic field, Ω is the ion magnetization parameter defined below, and the unknown fields are $\Phi(x,t)$, $n_i(x,t)$, $n_e(x,t)$ and $\mathbf{u}(x,t)$.

One more equation is required to determine the upstream potential $\Phi_0(t)$. That equation is the ambipolarity condition $\nabla \cdot \mathbf{J} = 0$ where the total current \mathbf{J} includes electron, ion and displacement currents. Integrating over the volume and including the source contribution at the midplane one obtains

$$J_{x1} - J_{x2} = -2J_{dc} b_x \quad (5)$$

where J_{dc} is the dimensionless injected DC current, normalized to the ion saturation current, $n_{i0} e c_s$ and $b_x = \mathbf{B} \cdot \mathbf{e}_x / B$. It can be shown that J_{dc} must lie in the range $|u_{||0}| - \mu \leq J_{dc} < |u_{||0}|$ where $\mu = (m_i / 2\pi m_e)^{1/2}$ and $|u_{||0}| = |\mathbf{b} \cdot \mathbf{u}(x=L)| \geq 1$. Here the x component of the current at plate 1 is given by [25]

$$J_{x1} = \mu b_x \exp(V_1 - \Phi_0) + n_{i1} u_{x1} - \partial_x \partial_t \Phi_1 \quad (6)$$

where subscript 1 indicates evaluation at the location of plate 1 and in Eq. (5) J_{x2} is determined by symmetry as $J_{x2}(\omega t) = -J_{x1}(\omega t + \pi)$. [25] The three terms in Eq. (6) are respectively the current density of electrons, ions and the displacement current. (In this work, there is no explicit use of a dielectric tensor. All dielectric properties of the plasma are modeled directly by the plasma response contained in Eqs. (1) – (4). Since the sheath problem is both nonlinear and non-neutral, textbook dielectric properties are not applicable.)

In addition to Φ_0 which determines the RF “rectified” DC potential $\langle \Phi_0 \rangle$, the other output quantity of interest is the dimensionless admittance parameter y defined by

$$y = \frac{2\langle J_{x1} \cos \varphi \rangle}{V_{\text{rf}}} + \frac{2i\langle J_{x1} \sin \varphi \rangle}{V_{\text{rf}}} \quad (7)$$

where $\varphi = \omega t$ is the RF phase and $\langle \dots \rangle$ indicates an average over φ on $[0, 2\pi]$. The boundary conditions are $n_{i0} = 1$, $\Phi(x=0) = -\xi \cos(\omega t)$, $\partial_x \Phi(x=L) = 0$ and $\mathbf{u}(x=L) = u_{\parallel 0} \mathbf{b}$ where, $\xi = eV_{\text{pp}}/(2T_e)$ is the dimensionless zero-peak RF voltage driving the plate. In this section 3, NoFlu results use the source velocity $u_{\parallel 0} = -1.1$ and the ions are hydrogen ($m_i/m_e = 1836$). To make contact with earlier pure capacitive sheath models, the effective capacitive admittance is given by $\text{Im}(y)$ and the effective (dimensionless) sheath width is therefore $\Delta = -i\omega/\text{Im}(y)$. However, Δ does not play a fundamental role in the present formalism.

The dimensionless input parameters of the model are $\hat{\omega} = \omega/\omega_{\text{pi}0}$, $\hat{\Omega} = \Omega_i/\omega_{\text{pi}0}$, b_x , ξ and J_{dc} . Note that $\Omega_i/\omega_{\text{pi}0} = \lambda_{\text{de}0}/\rho_s$ where $\rho_s = c_s/\Omega_i$ is the ion sound radius and $\Omega_i = ZeB/(m_i c)$ is the ion cyclotron frequency, so that $\hat{\Omega}$ is the sheath ion magnetization parameter. Except for Sec. 4, most of the points of this paper can be made for perpendicular sheaths, i.e. $b_x = 1$ for which the ion magnetization parameter does not enter. In the remainder of this paper dimensionless units will be employed unless otherwise specified, and the ‘‘hat’’ notations on $\hat{\omega}$ and $\hat{\Omega}$ will be dropped. Thus, the model generalizes the one in Refs. [25,26] by J_{dc} but is otherwise identical.

3. Numerical results

3.1. Sample spatial structure of the sheath

The space-time structure of RF sheaths in the NoFlu model has been discussed in detail in previous work.²⁵ Here we present a single example as a brief review, to provide context for the topics which follow.

Figure 2 shows the spatial structure of an RF sheath for the parameters $\omega = 2.51$, $b_x = 1$, $\xi = 10$ and $J_{\text{dc}} = 0.90$. This is the same case that will be shown later in figures 4(d)-(f) to illustrate the temporal waveforms. The choice of parameters here and in other cases shown in the paper was not motivated by a particular experiment but rather to best illustrate the underlying physical mechanisms and sheath behaviors in various regimes. Nevertheless, this case represents a plausible experimental situation: the magnetic field is parallel to the surface normal ($b_x = 1$), such as might occur on the sides of a limiter; the RF frequency is a bit above the lower hybrid frequency (which is close to $\omega_{\text{pi}0}$), and the RF voltage at the sheath is $10 T_e$. For example, in Alcator C-Mod, at 80 MHz, the density implied by $\hat{\omega} = 2.51$ would be $n_e = 0.18 \omega^2 = 4.6 \times 10^{16} \text{ m}^{-3}$ which is in the range of densities explored in Fig. 14 of Ref. [9] and the RF sheath potential would be 100 V for the quoted temperature of $T_e = 10 \text{ eV}$. Of course, the density varies over orders of magnitude in the scrape-off layer; higher density cases (lower $\hat{\omega}$) are considered in other examples.

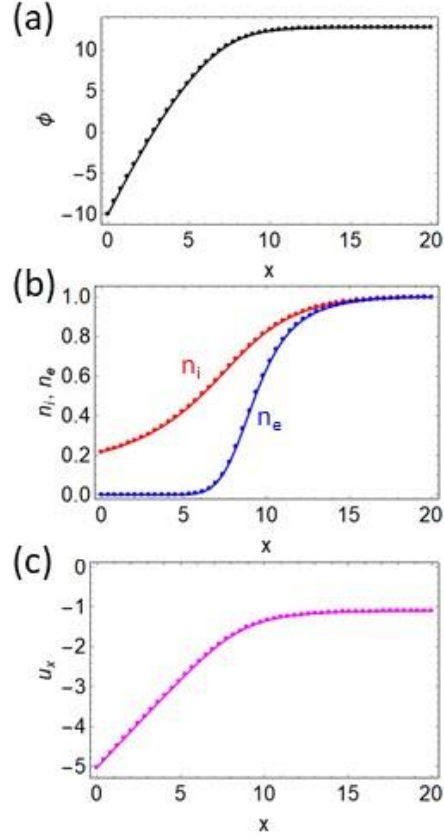


Figure 2. Sample spatial structure of an RF sheath, from the NoFlu code, illustrated at the time in the RF phase for which the sheath width is maximum. The wall is at $x = 0$ and upstream plasma conditions pertain at $x = 20$. Results are in dimensionless variables. See the text for plasma and RF parameters. Shown are: (a) electrostatic potential, (b) ion and electron densities and (c) fluid velocity normal to the wall.

The plots in Figure 2 are shown at the RF phase $\omega t = 0$ where the RF applied voltage at the left plate is at a minimum, $V_1 = -10$ (T_e), hence the sheath has its maximum width. It is evident from the plots that the non-neutral sheath extends out to about $x \sim 12$ (Debye lengths). Upstream, at $x = 20$, the quasi-neutral plasma attains a potential which is a few (T_e) above the $V_2 = +10$ potential that is anti-symmetrically applied at the right plate. The upstream plasma flow velocity is $u_x = -1.1$ (c_s), set by the boundary condition. As the ions move towards the wall the flow accelerates through the potential drop to about -5 (c_s) at the wall. At the wall, the negative potential excludes most of the electrons through the Boltzmann relation, Eq. (2).

3.2. DC current and frequency scans

We continue with one of the main results of this paper, the effect of DC current flow through the sheath on the DC “RF rectified” potential and on the RF sheath admittance. The results of a DC current scan are shown in figure 3 for both the NoFlu and hPIC codes. The dimensionless parameters for this scan are $\omega = 2.51$, $b_x = 1$ and $\xi = 10$ where we recall that ξ is the zero-to-peak voltage divided by T_e . Consequently, this case is for a moderately high frequency sheath and a high RF voltage.

From figure 3(a) it is seen that as J_{dc} increases towards more positive values, the DC potential difference between the plasma and the plate, $\langle\Phi_0\rangle$, increases. This is as expected: larger Φ_0 confines more electrons in the plasma, decreasing the electron particle flow to the plate, and thereby increasing the net DC current to the plate. There is a small offset between the hPIC results (large filled disks) and the NoFlu results (continuous curves) which will be discussed in Sec. 3.3. It results from differences in the particle source presheath models in the two codes; it is not an RF specific effect. Here and in figure 3(b) the red dotted curves are obtained from parametrized fits. These will be discussed in section 4.

Figure 3(b) shows the effect of J_{dc} on the RF sheath admittance parameter y . As J_{dc} increases towards more positive values, the magnitudes of both the real and imaginary parts of y decrease. The real part of y is primarily controlled by the electron current, which being suppressed at larger J_{dc} , results in reducing $\text{Re } y$. The imaginary part of y primarily comes from the displacement current, i.e. sheath capacitance. At larger J_{dc} where Φ_0 is larger, the sheath width broadens, reducing the capacitive current. The break-out of the admittance into electron, ion and displacement components as calculated by NoFlu is shown in figure 3(c). There is a significant electron contribution to $\text{Im } y$ at large negative values of J_{dc} which is also discussed in section 4. Finally, the agreement between hPIC and NoFlu for y is excellent, which suggests from Eq. (5) that the time-dependent current waveforms from the two codes may also agree well. This is examined next.

Waveforms for a complete RF period are shown in figure 4 for the two most extreme cases of J_{dc} depicted in figure 3. For the case of $J_{dc} = -3.13$ where the plates draw excess electrons, Φ_0 is not only lower on average in figure 4(a) compared to 4(d) but the minimum value is much lower. This is the time in the RF cycle when most of the electrons are lost. In both cases Φ_0 shows a significant 2ω harmonic that is a consequence of the double plate geometry. In this geometry the central potential must ride about the maximum voltage at either sheath.

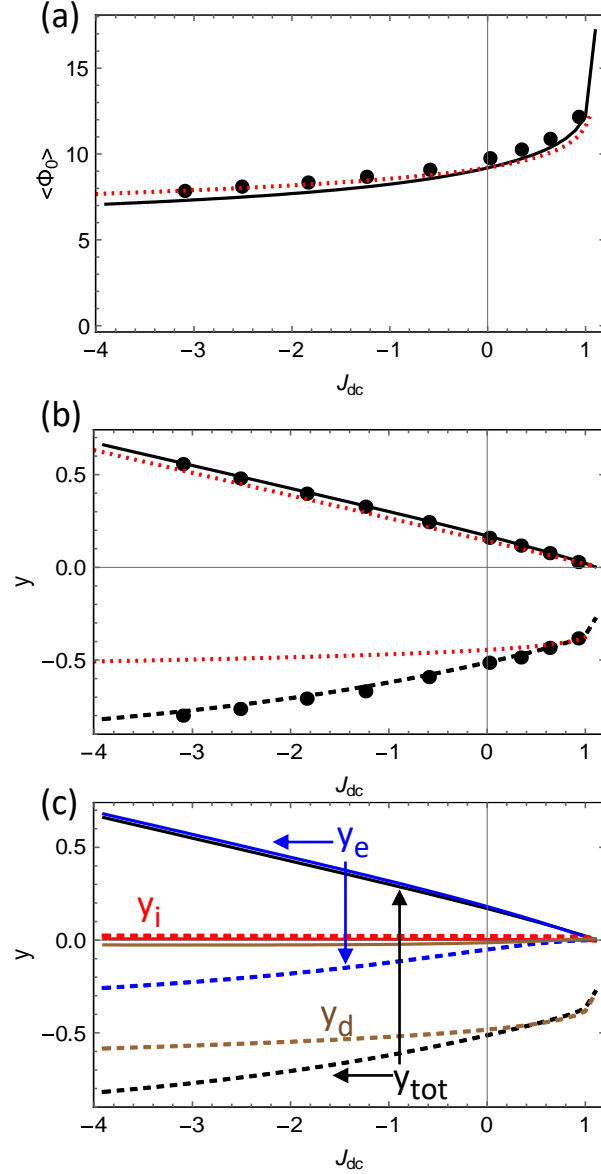


Figure 3. (a) Rectified upstream DC potential (b) sheath admittance parameter and (c) break-out of the admittance for a DC current scan. NoFlu results are shown with a continuous ($\langle \Phi_0 \rangle$ and Re y) or dashed (Im y) line and hPIC results are shown as discrete filled disks. In (a) and (b) the dotted red curves are parametrized fits discussed in section 4. All results are in normalized units.

The panels in figures 4(b) and (e) show the break-out of the current lost to the left plate with the sign convention that ion current, resulting from flow in the negative x direction is negative. Strong nonlinearity in the system comes from the exponential in the Maxwell-Boltzmann electron response. Thus, figure 4(b) in which electron current is dominant, shows nonlinear waveforms. In contrast, figure 4(e) for large positive J_{dc} is dominated by displacement current and is much more

sinusoidal. Panels 4(c) and 4(f) show the total current leaving the plasma summed over both plates, with the sign convention that net loss of ions from the plasma is positive. Here we can see that the total current (black curves) is indeed constant at twice the specified value of J_{dc} . The larger PIC noise evident in figures 4(e) and (f) is related to approaching the physical singularity that would occur if one draws all of the available upstream ion current, i.e. the ion saturation current. This increases the sensitivity of the system and the numerical noise from the charge conservation algorithm. [41]

In addition to elucidating the physics behind these cases, figure 4 illustrates the excellent cross-code comparison of current waveforms between the hPIC and NoFlu codes. This explains the agreement in the admittance. For the central potential in figures 4(a) and (d) we again note a systematic offset to be discussed in Sec. 3.3. For hPIC, a time dependent code, the illustrated waveforms were extracted from the last complete RF cycle in the simulation.

Figure 5 illustrates how the waveforms depend on frequency and provide additional cross-code verification between hPIC and NoFlu. For these cases $J_{dc} = 0$ and $\xi = 10$. At low frequencies the electron current tends to dominate the total RF sheath current making the waveforms quite nonlinear. In contrast the displacement current dominates at high frequencies. These trends are similar to what was seen in the J_{dc} scan at large negative and positive values in figure 4.

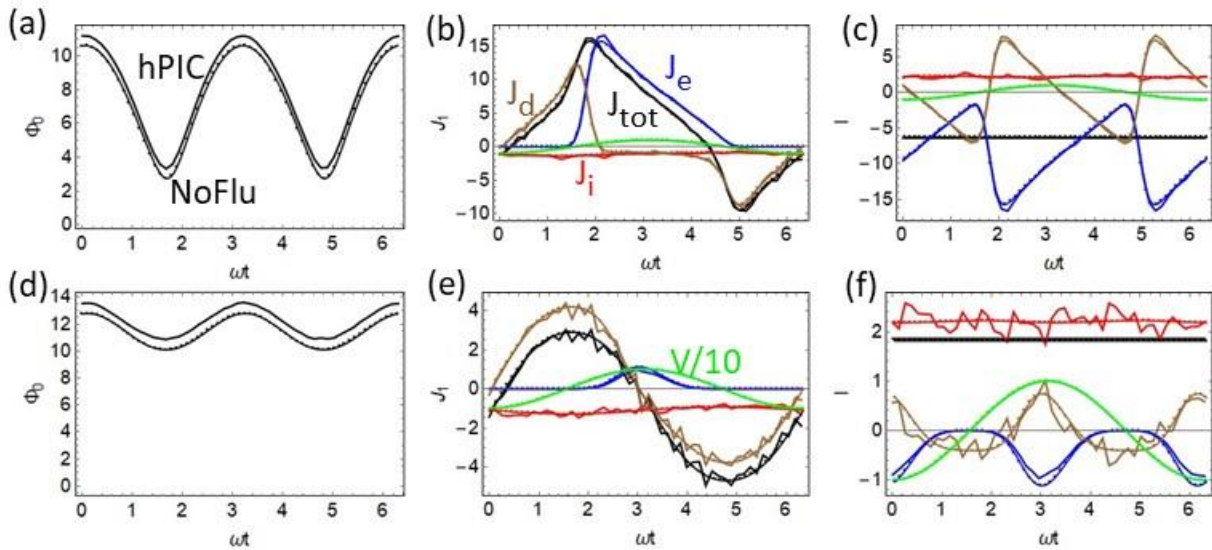


Figure 4. DC current carrying sheath waveforms for $J_{dc} = -3.13$ (top row) and $J_{dc} = 0.90$ (bottom row). Left to right, columns show upstream potentials (left column), current waveforms at the left plate (middle column) and total current leaving the plasma summed over both plates (right column). Smooth curves with small dots are NoFlu results, the more jagged current waveforms are from hPIC. All results are in normalized units. The color scheme for the individual current contributions is consistent in all the panels and in subsequent figures.

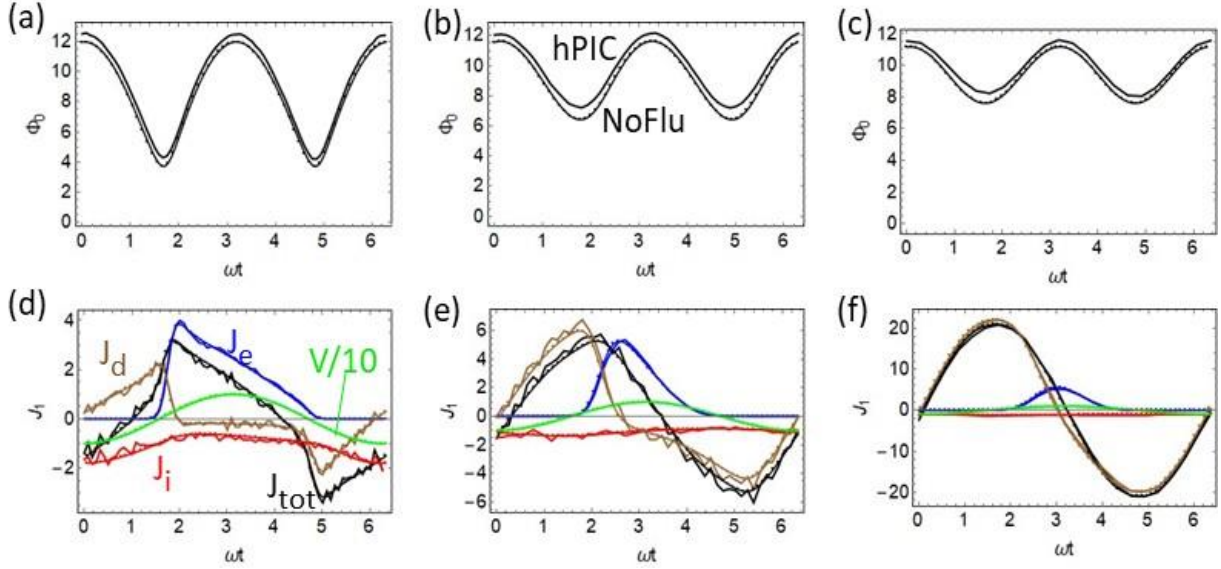


Figure 5. Upstream potentials (top row) and current waveforms at the left plate (bottom row) for three different frequencies $\omega = 0.57$ (left column), $\omega = 2.25$ (middle column) and $\omega = 11.1$ (right column). Smooth curves with small dots are NoFlu results, the more jagged current waveforms are from hPIC. All results are in normalized units.

3.3. Kinetic ion effects

One motivation for the NoFlu-hPIC cross-code comparisons was to assess the role of kinetic ion effects present in hPIC but not in the NoFlu model. As can be seen from the comparisons shown so far, kinetic ions seem not to significantly affect the RF rectified potential or the admittances for the cases shown. This is not entirely unexpected since (i) rectification is present in the first place to improve the confinement of electrons in the plasma, while the ion dynamics is mainly fluid flow at sonic or supersonic speeds to the plate, and (ii) the admittance in most cases is insensitive to the RF ion current since the ions move slowly. Rather, the admittance is typically dominated by either the electron or the displacement current, (iii) the most interesting RF cases from a practical point of view are for $eV_{\text{rf}} \gg T_i$. However, some differences between the models exist for these cases and are worth exploring.

As previously noted, all the cases show a small offset between hPIC and NoFlu in the upstream plasma potential Φ_0 , with the hPIC result exceeding the NoFlu result by about 0.5 to 0.7 in dimensionless units, i.e. relative to T_e . This difference can be traced to the additional contribution of the presheath, which is present in the hPIC simulations. For example, for the case $\omega = 0.5$ at $\omega t = 0$, the measured presheath potential drop in hPIC is 0.575 in dimensionless (T_e/e) units, which is within the range of potential offsets between the two codes. In NoFlu, plasma is injected towards each plate at $\pm 1.1 c_s$ at the midplane location $x = L$ in figure 1. In hPIC plasma is

sourced throughout the entire volume with a mean initial velocity of zero and a thermal ion distribution. For the cases shown so far, the injected ion temperature used in hPIC was $T_i = T_e = 10$ eV. (Note, however, that ion acceleration cooling, discussed in connection with figure 8, occurs in hPIC [36].) Thus, a quasi-neutral source presheath must be formed in the hPIC model to accelerate the ions up to sonic speeds before entering the non-neutral sheath. This presheath results in a presheath potential which adds to the potential across the non-neutral sheath and results in the observed small offset in $\Phi_0 \equiv \Phi(x=L)$ between the results of the two codes. The precise value of the presheath potential expected in experiments requires global modeling beyond the scope of this paper since it depends on the upstream plasma conditions. Thus, the observed offset in Φ_0 is not an RF specific effect and is not even specifically an ion kinetic effect, although there may be kinetic influences.

To explore the role of ion temperature in more detail we constructed an extreme case, mostly of academic interest, with $eV_{pp} = 20$ eV $\ll T_i = 100$ eV. Dimensionless parameters for this case were $\omega = 0.44$, $b_x = 1$, $\xi = 1$, $J_{dc} = 0$ and $T_i/T_e = 10$. Unlike strong RF cases where the ion motion is dominantly in response to the RF and rectified sheath fields, we expect this case to be dominated by ion thermal effects.

The spatial profiles of normalized potential, electron and ion density and ion velocity in the sheath region are shown in figure 6 for this case, again comparing hPIC and NoFlu results. The time slice shown is when the potential at the left plate is at a minimum, so that the sheath is at its largest width. Here, in this high T_i simulation, the potential offset in figure 6(a) is lower than that from NoFlu. This may be understood from standard static fluid sheath theory: the zero-current condition for the sheath potential drop with finite T_i is $\Delta\Phi = \ln[\mu/(1+T_i/T_e)^{1/2}]$. The T_i correction factor $-0.5 \ln(1+T_i/T_e) \approx -1.2$ is close to the potential difference of -0.9 between the two models at the sheath edge $x \approx 8$; the remaining discrepancy may be attributed to kinetic effects including ion cooling.

Figure 6(b) shows that the non-neutral sheath, where n_e and n_i differ, occupies the same location in the two models. However, the density at the sheath entrance is much lower in hPIC when normalized to its far upstream value. The inset shows that the quasi-neutral density rises to a normalized upstream value of 1 on a longer spatial scale of order 200 Debye lengths. The density drop in the hPIC result is again consistent with static fluid sheath theory which predicts a presheath density drop of $1/2$ between the upstream stagnation point and the sheath edge. [44]

Finally, the ion velocity at the sheath edge in Fig. 6(c) is about $-2.5 c_s$ (recall c_s is the cold ion sound speed). This is roughly $-2.5/(1+T_i/T_e)^{1/2} \approx -0.8$ of the isothermal warm ion sound speed, close to, but a bit smaller in magnitude than the fluid Bohm condition. The difference is likely of kinetic origin. It is important to note that these differences are not RF specific: they are all qualitatively understood from static fluid sheath theory.

Remarkably, even with these substantial differences in spatial sheath structure between the models, the RF current waveforms vs. RF phase (not shown), when compared using the procedure of section 2.3, are in almost as good agreement as in those shown in figures 4 and 5. This observation is in line with the fact that T_i scans of the hPIC admittance in the regime $0 < T_i \leq T_e \ll eV_{rf}$ were shown to be almost independent of T_i .³⁹

While the preceding may suggest that kinetic ions are not essential for reasonably accurate modeling of rectification and sheath admittance, it should be pointed out that our comparison explores a limited parametric domain. One can well imagine other cases, perhaps near the ion plasma frequency or, for a tilted magnetic field, the ion cyclotron frequency and its harmonics, where ion kinetic effects may prove to be more important. For example, Riyopoulos predicted unstable ion orbits near the ion cyclotron harmonics. [45] Another entirely different parameter regime is that of grazing sheaths for which the magnetic field is nearly tangent to the surface. In cases where the angle between the magnetic field and the surface normal is near $\pi/2$, or its complement satisfies $\theta < (2\pi m_e/m_i)^{1/2}$ the sheath may transition from being ion rich to being electron rich, and ion scrape-off from finite gyro-radius effects becomes important. Such cases are completely outside the scope of the present paper.

3.4. Kinetic electron effects

So far, all of the results in this paper have been obtained with the Boltzmann electron model, Eq. (2). In this section, the Vorpil code is employed to carry out a comparison of the Boltzmann model with a more complete model using kinetic electrons, and also retaining kinetic ions.

Figure 7 shows waveforms in NoFlu and Vorpil for a case with the parameters $\omega = 0.54$, $b_x = 1$, $\xi = 10$ and $J_{dc} = 0$. For these parameters, it is easily verified that the nominal condition for Boltzmann electrons, $\omega\Delta/(b_x v_{te}) \sim 0.15 < 1$, is satisfied. Here $\Delta \sim 12$ (Debye lengths) is the nominal RF sheath width (i.e. the region where n_e and n_i differ significantly; see e.g. figure 2 which is qualitatively similar to the case at hand) and $v_{te} = 43$ (c_s). This condition states that the electrons, which are tied to the field lines, can move across the sheath more quickly than the wave oscillates. Boltzmann electrons provide an instantaneous density and current response to the electric field whereas kinetic electrons include inertial effects.

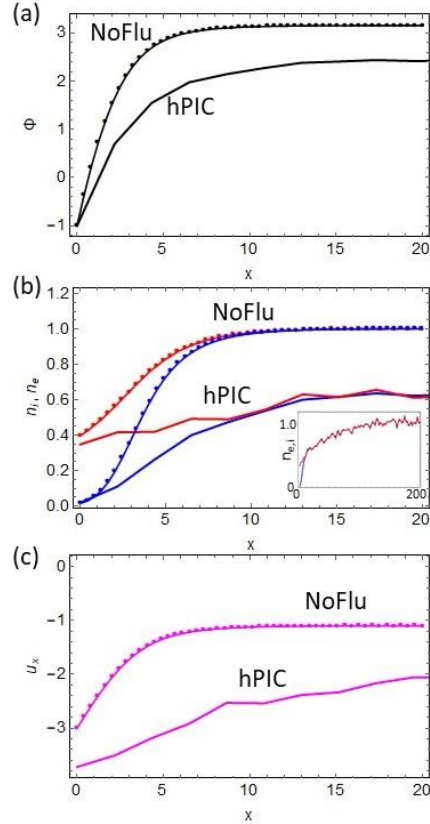


Figure 6. Spatial profiles of (a) potential, (b) ion and electron density normalized to their far upstream values and (c) flow velocity in the vicinity of the non-neutral sheath. The time instant shown is at the RF phase $\omega t = 0$ when the RF plate potential is at a minimum. The inset in (b) shows the density profiles on a larger scale on which the density ultimately achieves a normalized value of 1. All results are in normalized units.

Two Vorpil simulations, runs 41 and 42, were performed with the electrons sourced differently in each case. Run 41 had a spatially dependent electron reloading rate that was constant in time. For this case, Maxwellian electrons were loaded with thermal velocity v_{te} corresponding to $T_e = 10$ eV and electrons on the left (right) half of the domain were also given a mean flow of v_{te} to the right (left). Run 42 had a time-dependent reloading rate that was constant in space. Maxwellian electrons were again loaded with $T_e = 10$ eV but with a flow of $3v_{te}\cos(\omega t)$, out of phase with the applied RF potential. Steady-state electron distributions in the two runs were found to exhibit little mean flow and did not differ substantively from one another despite the differences in the loading scheme. In both cases Maxwellian ions were loaded with thermal velocity v_{ti} corresponding to $T_i = 10$ eV; ions on the left (right) half of the domain were also given a mean flow of v_{ti} to the right (left).

It is evident from figure 7 that the NoFlu Boltzmann-electron simulations capture the main features of both of these Vorpil simulations, but there are detailed and interesting differences.

Examining the upstream potential waveforms in figures 7(a) and (d) there is again an offset between NoFlu and Vorpall with the Vorpall kinetic electron results showing a lower value of $\langle\Phi_0\rangle$. See also figure 8(a). This difference has been traced to the fact that in the kinetic model the electrons cool rapidly. The cooling, present also in static sheaths [44] results from the fact that it is always the electrons in the tail of the distribution, i.e. with the energy $E_e = m_e v^2/2 - e(\Phi - \Phi_0) > T_e$ that escape the potential barrier provided by the sheath. Cooling occurs because sourcing the electrons at T_e does not fully replace the lost energy. The dramatic cooling effect is shown in the profiles of figure 8(c). Here a local effective T_e is determined from the average electron density in the flow frame. What this means for the present comparison of Φ_0 rectification driven by the RF is that one should correct for the fact that the thermal sheath potentials are different in NoFlu and Vorpall.

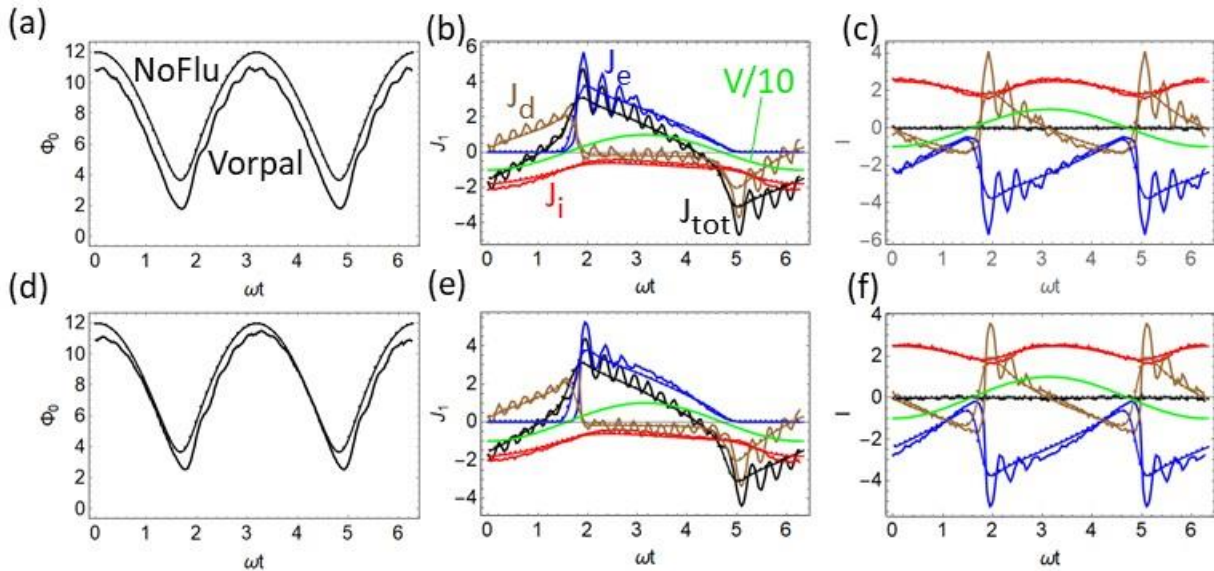


Figure 7. Comparison of sheath waveforms in NoFlu and Vorpall, where the Vorpall simulations employed kinetic electrons and ions. Left to right, columns show upstream potentials normalized to $T_e = 10$ eV (left column), current waveforms at the left plate (middle column) and total current leaving the plasma summed over both plates (right column) with currents normalized to the NoFlu ion saturation current. Smooth curves with small dots are NoFlu results, the more structured current waveforms are from Vorpall. The top row is for Vorpall run 41 and the bottom row is for run 42. The NoFlu data is the same in both cases.

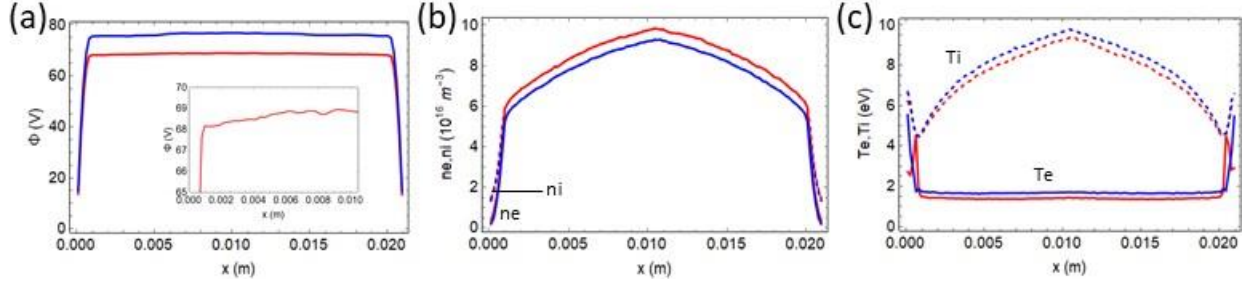


Figure 8. Time-averaged spatial profiles of (a) potential, (b) ion and electron density and (c) ion and electron temperature for the same two Vorpall simulations used in Fig. 7. The color coding indicates how the electrons are sourced: run 41 with spatially dependent source (red) and run 42 with time dependent source (blue). The inset figure in (a) shows an expanded view of the presheath potential in the left half of the domain for run 41. Dimensional (unnormalized) results are shown in this figure.

Reverting to dimensional units for this correction, the NoFlu run, mapped to $T_e = 10$ eV, had a total upstream DC potential $\langle \Phi_0 \rangle = 85$ V of which we may attribute an amount $T_e \ln[m_i/(2\pi m_e)] = 2.8 T_e/e = 28$ V to the thermal sheath. This leaves the RF rectification contribution $V_{\text{rect}} = \langle \Phi_0 \rangle - 2.8 T_e/e = 57$ V as the result from NoFlu. For Vorpall run 41 we find $\langle \Phi_0 \rangle = 69$ V. Again, splitting this into RF rectification and thermal sheath contributions, $\langle \Phi_0 \rangle = V_{\text{rect}} + 2.8 T_e/e$, we find that an effective electron sheath temperature of $T_e = 4.1$ eV would give the same RF rectification contribution of 57 V as obtained with NoFlu. Referring to figure 8(c), 4.1 eV is indeed close to the electron temperature at the sheath entrance ~ 4.5 eV, although T_e varies too rapidly in the sheath region for a more quantitative assessment. A similar analysis for Vorpall run 42 would suggest an effective T_e of 6.9 eV, qualitatively consistent with the higher T_e observed in run 42, although figure 8(c) gives a time-averaged T_e at the sheath entrance closer to 5.6 eV.

The other difference between NoFlu and both of the Vorpall runs is apparent in the high frequency oscillations in J_e , J_d and J_{tot} in figures 7(b) and (e) and also in J_e and J_d in figures 7(c) and (f). The origin of these oscillations may be traced to electron inertia, which is the physics added in a kinetic model that is lacking in the Boltzmann model. Inertia permits ω_{pe} electron plasma oscillations which exchange energy with the displacement current electric field. In run 41, the frequency of the oscillations is $\omega_{\text{osc}} \sim 2.5 \times 10^9$ /s or about 16 times that of the rf frequency. This frequency is equal to ω_{pe} at a density of $n_e = 1.9 \times 10^{15} \text{ m}^{-3}$ which is very close to the time-averaged density at the wall for this case, $n_{e_w} \sim 2.1 \times 10^{15} \text{ m}^{-3}$. We have verified that the ω_{pe} oscillations are generated near the wall, extend into the presheath plasma and decay towards the center of the domain. The frequency spectrum of these high frequency oscillations is broad enough that it overlaps with multiple harmonics in the range of 10 to 20. Comparing the oscillations in

runs 41 and 42, it is evident and not surprising that the precise magnitude and form of oscillations is sensitive to the details of the electron fueling.

A few other results of the Vorpil simulations for the time-averaged profiles are shown in figure 8. The inset in figure 8(a) shows that there is a presheath potential drop of approximately $0.5 T_e$ between the sheath entrance and the midplane. There is a corresponding presheath quasi-neutral density drop in figure 8(b). Figure 8(c) shows that the ions also cool from their source energy of 10 eV as they accelerate towards the wall. Ion acceleration cooling [36,44], which converts thermal ion energy into flow energy, occurs in both hPIC and Vorpil, and results in an approximate factor of two decrease in T_i from the source to the sheath entrance. Here an effective T_i is determined from the average ion energy in the flow frame. The time-dependent reloading case (run 42, blue) maintains higher electron and ion temperatures than the time-independent reloading case (run 41, red), likely because the source in the former case includes additional kinetic energy. On the other hand, the density is lower in case 42. We speculate that the lower density in case 42 is because the loss rate, which scales with nc_s must equal the source rate, and c_s is higher in run 42. (Recall that particles of both species are loaded at a fixed rate.)

We conclude from this section that the cross-benchmarking between NoFlu and Vorpil also successfully verifies these codes within some limitations. The most important and interesting limitations are the additional physics provided by the kinetic electron model. The inertia included in the kinetic model gives rise to electron plasma oscillations in the Vorpil simulations, oscillations which are outside the NoFlu Boltzmann-electron model. From the two Vorpil simulations with different loading methods, it can also be concluded that the details of the electron response are sensitive to the actual source. Modeling the electron sources in a real tokamak experiment is well beyond the scope of this work, and would likely require an integrated model taking into account particle and electron energy transport across as well as along field lines.

4. Analytical results and parametrization fits

The goal of this section is to propose and test some semi-analytical fits to the DC sheath potential $\langle\Phi_0\rangle$ and RF admittance parameter y in the presence of net DC current. A procedure for these semi-analytical fits with zero net DC current was described in Ref. 26. In Ref. 39 the effect of net DC current on $\langle\Phi_0\rangle$ and y was briefly treated in the low frequency limit. It turns out that the low frequency limit motivates a method for a procedure that works quite well in the general case. We first review that procedure here.

In the low frequency limit, $\omega \ll 1$, we can drop the displacement current in J_{x1} , Eq. (6), and use the symmetry of the problem, $J_{x2}(\omega t) = -J_{x1}(\omega t + \pi)$ in Eq. (5). The ion current is simplified by integrating Eq. (3) in x after dropping the time derivative to obtain $n_{i1}u_{x1} = n_{i0}u_{x0} = u_{x0} =$

$b_x u_{||0}$, where $n_{i0} = 1$ in dimensionless variables. After some algebra Eq. (5) may be solved for the upstream potential to yield

$$\Phi_0 = \ln \left[\frac{\mu \cosh(\xi \cos \varphi)}{|u_{||0}| - J_{dc}} \right] \quad (8)$$

where the symmetry relations $V_2(\varphi) = V_1(\varphi + \pi) = -V_1(\varphi)$ and $\Phi_0(\varphi) = \Phi_0(\varphi + \pi)$ have been used and $\varphi = \omega t$ is the RF phase. From this waveform, $\langle \Phi_0 \rangle$ can be calculated numerically for given μ and ξ by performing the periodic average over φ . Since $|u_{||0}| - J_{dc}$ is independent of φ , the net result is that the effect of J_{dc} may be accounted for analytically given the parametrized results for the $J_{dc} = 0$ case. [26]

The electron admittance is obtained from Eq. (7) with $J_{x1} \rightarrow J_{ex1}$, i.e. the first term in Eq. (6). In this limit $\text{Im } y_e = 0$ and the real part is given by

$$\begin{aligned} y_e &= \frac{2\mu b_x}{\xi} \left\langle e^{\xi \cos \varphi - \Phi_0} \cos \varphi \right\rangle \\ &= \frac{4b_x}{\xi} \left\langle \frac{\cos \varphi}{1 + e^{-2\xi \cos \varphi}} \right\rangle (|u_{||0}| - J_{dc}) \end{aligned} \quad (9)$$

where the second form of y_e in Eq. (9) makes explicit use of the result for Φ_0 in Eq. (8). Again, it is found that the effect of J_{dc} may be accounted for analytically, if y_e is known for the $J_{dc} = 0$ case. J_{DC} also modifies y_i and y_d indirectly since each of these admittance contributions depends on $\langle \Phi_0 \rangle$ using functional forms given explicitly in Ref. [26].

The preceding derivation of the effect of J_{dc} in the low frequency limit motivates the following quasi-static ansatz in the general frequency case.

$$\langle \Phi_0 \rangle = \langle \Phi_0 \rangle_{J_{dc}=0} - \ln \left(1 - J_{dc} / |u_{||0}| \right) \quad (10)$$

$$y_e = \left(1 - J_{dc} / |u_{||0}| \right) y_e|_{J_{dc}=0} \quad (11)$$

and the use of the modified $\langle \Phi_0 \rangle$ given by Eq. (10) for the calculation of y_i and y_d .

As a side comment, the alert reader will note that Eqs. (8) and (10) may be recast into the form of a standard sheath current-voltage relationship

$$\begin{aligned}
J_{\text{dc}} &= |u_{\parallel 0}| \left(1 - e^{-\langle \Phi_0 \rangle + \Phi_f} \right) \\
\Phi_f &= \ln \left[\frac{\mu \cosh(\xi \cos \varphi)}{|u_{\parallel 0}|} \right]
\end{aligned} \tag{12}$$

where Φ_f is the ‘‘floating potential’’. In the absence of RF, i.e. $\xi = 0$, and with $|u_{\parallel 0}| = 1$ (sonic flow) the usual floating potential is obtained, $\Phi_f \rightarrow \ln \mu$; with RF present, the floating potential is shifted [46]. Other current-voltage characteristics have also been proposed in the literature [15] and used to interpret RF sheath experimental results [4]. Details will depend on the specific model geometry. Here our immediate goal is to test the quasi-static ansatz results for RF rectification and impedance against the full nonlinear fluid model which includes displacement current and inertia.

These tests were performed using the NoFlu code for a total of 178 runs covering the following parameter ranges: $-4.901 \leq J_{\text{dc}} \leq 1.099$, $0.1 \leq \Omega \leq 16$, $0.05 \leq \omega \leq 8$, $0.2 \leq b_x \leq 1.0$ and $5 \leq V_{\text{pp}} \leq 20$. These runs were performed for deuterium plasmas on domain sizes ranging from normalized $L = 20$ (see figure 2) to $L = 80$ for oblique magnetized ion cases. The larger domain sizes are required in the latter cases to accommodate the magnetic presheath. Results are shown in figure 9.

It can be seen that the fits for $V_{\text{dc}} \equiv \langle \Phi_0 \rangle$ and $\text{Re } y$ are quite good. The fit for $\text{Im } y$ is qualitatively correct but less accurate. To explore the reason for this, the 12 cases with the largest deviations of the fits for $\text{Im } y$ were extracted from the database and highlighted in red. Analysis reveals that they correspond to input parameters with moderately high frequency, moderate to high RF voltage and/or large negative DC current. The moderate frequency range is expected because at low frequencies, $\omega < \omega_{\text{pi}}$ the imaginary part of the impedance is usually small and dominated by the real part from the electron response while at very high frequency the sheath is capacitive and dominated by displacement current. The other two conditions turn out to be just the conditions for which the waveforms are strongly nonlinear and non-sinusoidal. Nonlinear waveforms are a result of the large Φ variation in the Maxwell Boltzmann exponential function, a feature which is all the more dominant when large negative J_{dc} requires large electron current flow.

To further illustrate this point, figure 9 also shows with green dots the 6 cases with illustrated waveforms in figures 4, 5 and 7. The parametrized fits follow the trends of these cases. The particular case of the left-most data point in figure 3 (waveforms in the top panels of figure 4) is additionally highlighted with a green open circle. We can now understand why the parametrized (red dotted) curve in figure 3(b) for $\text{Im } y$ deviates from the code results at large negative J_{dc} . As is clear from figure 4(b) this is a case where the nonlinear waveforms are important and where the electron current contributes significantly to $\text{Im } y$. In fact, comparing figures 3(b) and (c) we can see that at large negative J_{dc} the parametrization captures the displacement impedance y_{d} quite

well, but fails to account for the additional contribution from $\text{Im } y_e$. It is not yet clear how to parametrize such strong nonlinearities, but also not yet relevant for the boundary condition in present day global RF simulations (see Discussion). A python module for calculating the parametrized DC potential and admittance is available from the lead author on request.

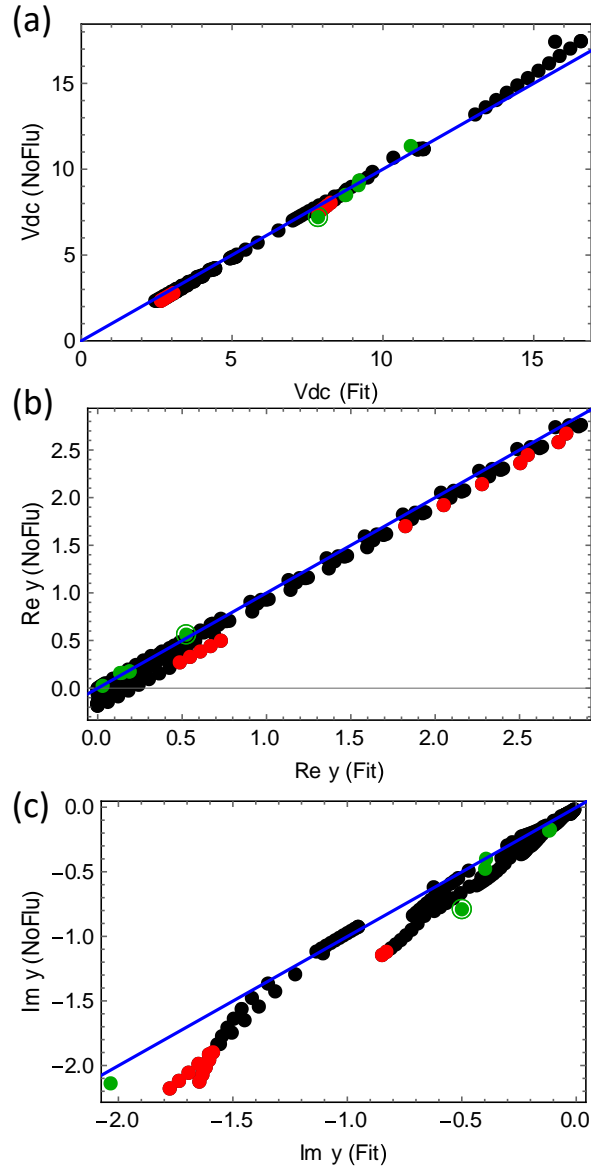


Figure 9. Comparison of fits to NoFlu code results for (a) upstream “rectified” DC potential, (b) real part of the admittance parameter, and (c) imaginary part of the admittance parameter. The diagonal blue line corresponds to a perfect fit. See the main text for a discussion of red and green data points. All results are in normalized units.

5. Discussion

As noted in the introduction, many experiments have observed DC current flow associated with the application of ICRF wave power. Modeling of these and other such experiments will hopefully be aided by the present paper, but is beyond its scope. A few comments can be made, however. In Ref. [29] Perkins emphasizes the important of current rectification, i.e. DC current flow through the sheath, in the analysis of high harmonic fast wave (HHFW) power losses in NSTX. It is noted there that ignoring rectified current may lead to underestimated heat fluxes and overestimated rectified voltages. Not surprisingly, the analysis of Fig. 3(a) and Eq. (8) shows that when the wall draws net negative current (i.e. electrons) the DC sheath voltage from RF rectification drops.

In a recent experiment on LAPD, DC currents flowing to a tungsten plate immersed in an RF plasma were measured. [31] In this case, both negative and positive DC currents were observed depending on the DC plasma potential. In general, the DC plasma potential at a particular sheath location may or may not be the result of local RF rectification processes. Rectification can also occur at remote locations that are magnetically connected to the point in question. [33] In the LAPD experiments of Ref. [31] it was argued that rectification at the RF antenna was the primary driver of the DC potential at the remote but magnetically connected tungsten plate. Fully predictive modeling of these types of situations require a global approach, where the DC and RF voltages and currents at many locations are coupled by global circuits and full wave RF solutions. Such tools for integrated modeling in realistic device geometry are envisioned and under development but not yet available. The present paper can only provide one piece of the global model. In Ref. [31] the DC plasma potential was in fact measured, not predicted, and in that smaller context it was possible to validate some aspects of the present approach. In particular, the RF sheath impedance that results from an independently specified DC sheath voltage was verified within some limitations.

The simplest approach to coupling a sheath impedance and rectification model to an RF code and to a DC circuit is to employ the parametrized fits of section 4. As noted there, these fits are not without accuracy caveats and have only been tested rather sparsely in the full five-dimensional parameter space. A particular accuracy issue was identified for cases with moderate frequency, high voltage and/or large negative DC current. This region of parameter space is associated with strongly nonlinear sheath current waveforms. Although this point is worthy of further exploration, it should be noted that most full wave RF codes in use today for tokamak modeling are linear and operate in the frequency domain at the fundamental frequency of the launched RF wave. They cannot in any case accurately model situations where strong sheath nonlinearity and harmonic generation are important.

It is possible to envision various extensions to the NoFlu model and/or additional more sophisticated applications of all of the models for RF surface interactions. In Ref. 14, Elias coupled a nonlinear fluid model (almost equivalent to NoFlu) to sputtering and impurity calculations by using mean energy and angle information from the fluid code to construct kinetic distributions. Direct use of both hPIC and Vorpal for calculating kinetic energy-angle ion distribution functions for RF surface interactions is also in progress. This approach could in principle also account for anisotropic energetic ion tails that might exist in the edge plasma.

It is expected that integrated modeling will be required to address RF surface interaction problems. The framework should make tools at various levels of sophistication and fidelity available to the modeler. For RF rectification and sheath impedance tools one could envision using everything from the parametrized fits, to NoFlu, hPIC or Vorpal to couple to RF full wave codes, with input upstream ion distribution functions available from Fokker-Planck codes and impurity release calculated from surface interaction and transport codes.

6. Summary and conclusions

In this paper we have studied the effect of DC current flow on the properties of an RF sheath, and compared RF sheath quantities of interest for three different RF sheath models: a cold ion nonlinear fluid code (NoFlu), a PIC code configured with kinetic ions (hPIC), and a PIC code with kinetic ions and kinetic electrons (Vorpal). Primary quantities of interest in this paper included the upstream RF voltage rectification and the RF sheath admittance. The paper generalizes earlier work using the fluid model on voltage rectification and RF impedance (or equivalently admittance) for sheaths with no net DC current.

The main results of this paper are to be found in figures 3, 4, 7 and 9 and in Eqs. (10) and (11). Figure 3 illustrated general trends for the dependences of RF sheath voltage rectification and RF sheath admittance on the DC current flow through the sheath. These trends were encapsulated approximately and analytically in Eqs. (10) and (11) and the resulting parametrization was compared with a large number of NoFlu numerical results in figure 9. Figures 4 and 7 compared NoFlu results with results from hPIC and Vorpal respectively. Although the agreement was quite good in both cases, some differences were noted. A small upstream offset in the electrostatic potential was attributed to different presheath potentials arising from different source models in the three codes. Finite T_i effects were found to be rather small on the voltage rectification and current waveforms (hence on the admittance) in the limit $T_i < eV_{rf}$, and electron inertia was found to introduce electron plasma oscillations into the sheath current waveforms.

A procedure for comparing the results of rather different physics models in NoFlu, hPIC, and Vorpal was presented in section 2.3. The procedure takes into account differences in the upstream ion velocity, sound speed and density that arise in the different models. This allows the

results of simple models such as NoFlu to essentially predict certain results from much more sophisticated and general models. It is not obvious that this would be possible. It apparently indicates that the particular aspects of the sheath being studied here (RF rectification and sheath admittance) are not sensitive to all of the details but rather depend on bulk parameters such as the net ion current and the total electron plus ion DC current striking the wall.

We have noted that experiments often observe DC currents driven by RF wave fields. These currents have been shown herein to affect the sheath voltage and admittance. By inference they will also directly affect the impact energy of ions for sputtering and the details of how the RF waves interact with the surfaces in terms of wave reflection and RF sheath power dissipation. It is hoped that the present work can therefore contribute to predictive integrated modeling of such processes in the future, and to the improvement of ICRF as a tool for the achievement of fusion energy as a power source.

Acknowledgements

This material is based upon work supported by the U.S. Department of Energy Office of Science, Office of Fusion Energy Sciences under Awards DE-FG02-97ER54392, DE-AC05-00OR2272 subcontract 4000158507, DE-SC0018141, DE-SC0018319 and DE-SC0018090-PO97564. Discussions with team members of the RF SciDAC project (Discovery through Advanced Computing Initiative: Center for Integrated Simulation of Fusion Relevant RF Actuators) are gratefully acknowledged.

The digital data for this paper can be found at <https://doi.org/10.5281/zenodo.3955183>

References

- [1] J.-M. Noterdaeme and G. Van Oost, *Plasma Phys. Control. Fusion* **35**, 1481 (1993).
- [2] S. J. Wukitch, M. L. Garrett, R. Ochoukov, J. L. Terry, A. Hubbard, B. Labombard, C. Lau, Y. Lin, B. Lipschultz, D. Miller, M. L. Reinke, D. Whyte, and Alcator C-Mod Team, *Phys. Plasmas* **20**, 056117 (2013).
- [3] V. Bobkov, M. Balden, R. Bilato, F. Braun, R. Dux, A. Herrmann, H. Faugel, H. Fünfgelder, L. Giannone, A. Kallenbach, H. Maier, H.W. Müller, R. Neu, J.-M. Noterdaeme, Th. Pütterich, V. Rohde, N. Tsujii, F. Zeus, H. Zohm and the ASDEX Upgrade Team, *Nucl. Fusion* **53**, 093018 (2013).
- [4] J. Jacquot, D. Milanese, L. Colas, Y. Corre, M. Goniche, J. Gunn, S. Heuraux, and M. Kubi, *Phys. Plasmas* **21**, 061509 (2014).
- [5] C. M. Qin, Y. P. Zhao, H. Q. Wang, X. J. Zhang, B. N. Wan, J.-M. Noterdaeme, F. Braun, V. Bobkov, H. Kasahara, E. H. Kong, L. Wang, Y. Shuai, Z. X. He, B. J. Ding, ICRF Team and EAST Team, *Plasma Phys. Control. Fusion* **55**, 015004 (2013).

- [6] Y. Corre, M. Firdaouss, L. Colas, A. Argouarch, D. Guilhem, J. Gunn, C Hamlyn-Harris, J. Jacquot, M. Kubic, X. Litaudon, M. Missirlian, M. Richou, G. Ritz, D. Serret and K. Vulliez, Nucl. Fusion **52**, 103010 (2012).
- [7] I. Cziegler, J. L. Terry, S. J. Wukitch, M. L. Garrett, C. Lau and Y. Lin, Plasma Phys. Control. Fusion **54**, 105019 (2012).
- [8] R.J. Perkins, J.-W. Ahn, R.E. Bell, A. Diallo, S. Gerhardt, T.K. Gray, D.L. Green, E.F. Jaeger, J.C. Hosea, M.A. Jaworski, B.P. LeBlanc, G.J. Kramer, A. McLean, R. Maingi, C.K. Phillips, M. Podesta, L. Roquemore, P.M. Ryan, S. Sabbagh, F. Scotti, G. Taylor and J.R. Wilson, Nucl. Fusion **53**, 083025 (2013).
- [9] R. Ochoukov, D. G. Whyte, D. Brunner, D. A. D’Ippolito, B. LaBombard, B. Lipschultz, J. R. Myra, J. L. Terry and S. J. Wukitch, Plasma Phys. Control. Fusion **56**, 015004 (2014).
- [10] K. Crombé, R. D’Inca, J. Jacquot, R. Ochoukov, M. Usoltceva, A. Kostic, F. Louche, D. Van Eester, A. Nikiforov, J. Moreno, S. Heuraux, S. Devaux, J. Moritz, E. Faudot, H. Fünfgelder, H. Faugel, F. Zeus and J-M. Noterdaeme, “IShTAR: a helicon plasma source to characterise the interactions between ICRF and plasma,” 26th IAEA Fusion Energy Conference, Kyoto, Japan, 17-22 October 2016, IAEA-CN-234/EX-P6-48.
- [11] M. J. Martin, W. Gekelman, B. Van Compernelle, P. Pribyl, and T. Carter, Phys. Rev. Lett. **119**, 205002 (2017).
- [12] J.R. Myra, D.A. D’Ippolito, D.A. Russell, L.A. Berry, E.F. Jaeger and M.D. Carter, Nucl. Fusion **46** S455 (2006).
- [13] D. A. D’Ippolito and J. R. Myra, J. Nucl. Mater. **415**, S1001- S1004 (2011).
- [14] M. Elias, D. Curreli, T. G. Jenkins, J. R. Myra, and J. Wright, Phys. Plasmas **26**, 092508 (2019).
- [15] L. Colas, J. Jacquot, S. Heuraux, E. Faudot, K. Crombé, V. Kyrtsya, J. Hillairet and M. Goniche, Phys. Plasmas **19**, 092505 (2012).
- [16] D. N. Smithe, D. A. D’Ippolito, and J. R. Myra, AIP Conference Proceedings **1580**, 89 (2014).
- [17] N. Bertelli, E.F. Jaeger, J.C. Hosea, C.K. Phillips, L. Berry, S.P. Gerhardt, D. Green, B. LeBlanc, R.J. Perkins, P.M. Ryan, G. Taylor, E.J. Valeo and J.R. Wilson, Nucl. Fusion **54**, 083004 (2014).
- [18] D. Van Eester, K. Crombé and V. Kyrtsya, Plasma Phys. Control. Fusion **55**, 055001 (2013).
- [19] J.R. Myra and D.A. D’Ippolito, Plasma Phys. Controlled Fusion **52**, 015003 (2010).
- [20] H. Kohno, J. R. Myra, and D. A. D’Ippolito, Phys. Plasmas **19**, 012508 (2012).
- [21] D. A. D’Ippolito, J. R. Myra, R. Ochoukov, and D. G. Whyte, Plasma Phys. Control. Fusion **55**, 085001 (2013).
- [22] H. Kohno, J. R. Myra, and D. A. D’Ippolito, Phys. Plasmas **20**, 082514 (2013).
- [23] W. Tierens, J. Jacquot, V. Bobkov, J.M. Noterdaeme, L. Colas and The ASDEX Upgrade Team, Nucl. Fusion **57**, 116034 (2017).
- [24] W. Tierens, G. Urbanczyk, L. Colas, and M. Usoltceva, Phys. Plasmas **26**, 083501 (2019).
- [25] J. R. Myra and D. A. D’Ippolito, Phys. Plasmas **22**, 062507 (2015).
- [26] J. R. Myra, Phys. Plasmas **24**, 072507 (2017).
- [27] R. Van Nieuwenhove and G. Van Oost, Plasma Phys. Cont. Fusion **34**, 525 (1992).

- [28] V. Bobkov, R. Bilato, L. Colas, R. Dux et al., EPJ Web of Conferences **157**, 03005 (2017).
- [29] R. J. Perkins, J.C. Hosea, M.A. Jaworski, R.E. Bell et al., Nuclear Materials and Energy **12**, 283 (2017).
- [30] R. J. Perkins, J. C. Hosea, G. Taylor, N. Bertelli et al., Plasma Phys. Cont. Fusion **61**, 045011 (2019).
- [31] J. R. Myra, C. Lau, B. Van Compernelle, S. Vincena and J. Wright, Phys. Plasmas **27**, 072506 (2020).
- [32] D.A. D'Ippolito, J.R. Myra, P.M. Ryan, E. Righi, J.A. Heikkinen, P. Lamalle, J.-M. Noterdaeme, and EFDA-JET workprogramme contributors, Nucl. Fusion **42**, 1357 (2002).
- [33] L. Lu, L. Colas, J. Jacquot, B. Després, S. Heuraux, E. Faudot, D. Van Eester, K. Crombé, A. Křivská, J.-M. Noterdaeme, W. Helou and J. Hillair, Plasma Phys. Control. Fusion **60**, 035003 (2018).
- [34] A. Ngadjeu, E. Faudot, L.Colas, S.Heuraux, J.Gunn, M.Kubič, J. Nucl. Mater. **415**, S1009 (2011).
- [35] E. Faudot, S. Heuraux, M. Kubic, J. Gunn, and L. Colas, Phys. Plasmas **20**, 043514 (2013).
- [36] R. Khaziev and D. Curreli, Phys. Plasmas **22**, 043503 (2015).
- [37] R. Khaziev and D. Curreli, Comp. Phys. Commun. **229**, 87 (2018).
- [38] C. Nieter and J. R. Cary, J. Comp. Phys. **196**, 448 (2004).
- [39] J. R. Myra, D. Curreli, M.T. Elias and T. G. Jenkins, AIP Conference Proceedings **2254**, 050008 (2020); <https://doi.org/10.1063/5.0013522>
- [40] E. Faudot, Phys. Plasmas **22**, 083506 (2015).
- [41] M. Elias and D. Curreli, J. Comp. Phys. **409**, 109320 (2020).
- [42] J. Drobny, A. Hayes and D. Curreli, D. N. Ruzic, J. Nucl. Mater. **494**, 278 (2017).
- [43] J. Drobny and D. Curreli, Comp. Mater. Science **149**, 301 (2018).
- [44] P. C. Stangeby, The Plasma Boundary of Magnetic Fusion Devices (Institute of Physics Publishing, Bristol, Philadelphia, PA, 2000).
- [45] S. Riyopoulos, Phys. Rev. Lett. **68**, 3303 (1992).
- [46] P. Chabert and N. Braithwaite, *Physics of Radio-Frequency Plasmas* (Cambridge, Cambridge University Press, 2011).

This report was prepared as an account of work sponsored by an agency of the United States Government. Neither the United States Government nor any agency thereof, nor any of their employees, makes any warranty, express or implied, or assumes any legal liability or responsibility for the accuracy, completeness, or usefulness of any information, apparatus, product, or process disclosed, or represents that its use would not infringe privately owned rights. Reference herein to any specific commercial product, process, or service by trade name, trademark, manufacturer, or otherwise does not necessarily constitute or imply its endorsement, recommendation, or favoring by the United States Government or any agency thereof. The views and opinions of authors expressed herein do not necessarily state or reflect those of the United States Government or any agency thereof.